Direct laser deposition of crack-free CM247LC thin walls

Alhuzaim, Abdullah; Imbrogno, Stano; Attallah, Moataz M.

DOI:
10.1016/j.matdes.2021.110123

Document Version
Publisher's PDF, also known as Version of record

Citation for published version (Harvard):
Alhuzaim, A, Imbrogno, S & Attallah, MM 2021, 'Direct laser deposition of crack-free CM247LC thin walls: mechanical properties and microstructural effects of heat treatment', *Materials and Design*, vol. 211, 110123. https://doi.org/10.1016/j.matdes.2021.110123

Materials & Design 211 (2021) 110123

Contents lists available at ScienceDirect

Materials & Design

journal homepage: www.elsevier.com/locate/matdes

Direct laser deposition of crack-free CM247LC thin walls: Mechanical properties and microstructural effects of heat treatment

Abdullah Alhuzaim [a,b], Stano Imbrogno [a], Moataz M. Attallah [a,*]

[a] School of Metallurgy and Material Sciences, University of Birmingham, Edgbaston, Birmingham B15 2TT, United Kingdom
[b] Mechanical Engineering Department, Jubail University College, Jubail Industrial City, Saudi Arabia

HIGHLIGHTS

- CM247LC Ni-superalloy experience cracking during direct laser deposition.
- Pulsed wave laser deposition successfully produced crack-free thin walls.
- A narrow process window was identified for successful deposition.
- Laser pulsing helps control the residual stress by reducing the heat input.
- Strain-age cracking during heat treatment was also avoided.

GRAPHICAL ABSTRACT

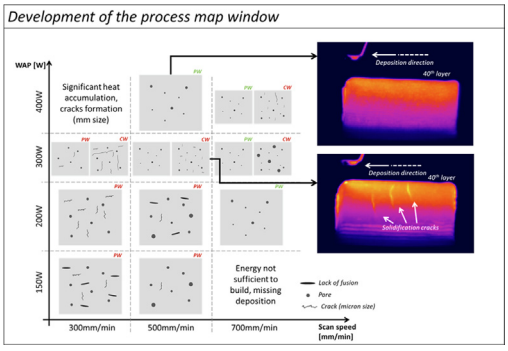

ARTICLE INFO

Article history:
Received 1 July 2021
Revised 14 September 2021
Accepted 22 September 2021
Available online 24 September 2021

Keywords:
Nickel Superalloy
CM247LC
Direct Laser Deposition
Microstructure
Mechanical properties

ABSTRACT

CM247LC is classified as a non-weldable Ni alloy due to the high Ti + Al content, which makes it susceptible to cracking. It is particularly prone to microcracking when processed by direct laser deposition (DLD). In this work, multiple single walls were manufactured by DLD in CM247LC using two different laser modes: continuous wave and pulse wave (PW). The manufactured walls were studied during processing and post-processing, and characterised by scanning electron microscopy, electron backscattered diffraction, thermal analysis and X-ray diffraction. The results indicate that crack-free conditions during the deposition process and the subsequent thermal processing can be achieved using the PW laser mode and that this can also lead to outstanding mechanical properties.

1. Introduction

Parts for submarine, aerospace and gas turbine engines, and nuclear reactors that need to withstand high temperatures while maintaining good mechanical properties and performance are usually manufactured using nickel-based superalloys. Among the materials that belong to this family, CM247LC is a valid choice due to its unique properties, like excellent resistance to chemical and mechanical degradation under thermal exposure [1]. The excellent mechanical properties at high temperature are also explained by the high γ' content of up to 67% volume fraction in the fully heat-treated condition. CM247LC has a chemical composition that is modified from that of MAR M247, and it is specifically designed for making directionally solidified turbine blades; however, it is one of the most difficult alloys to process by conventional fusion welding due to its crack susceptibility [2]. Additive manufacturing (AM) has become an innovative and valid manufacturing method owing to potential advantages such as waste reduction and enhanced design freedom, which consequently leads to a

* Corresponding author.
E-mail address: m.m.attallah@bham.ac.uk (M.M. Attallah).

https://doi.org/10.1016/j.matdes.2021.110123
0264-1275/

significant decrease in the buy-to-fly ratio. Moreover, the possibility of enhancing the efficiency and performance of components, such as turbine blades, has made AM a valid choice for industry, thanks to the ability to redesign components with geometrical and metallurgical features (e.g., internal cooling channels, gradual microstructure variation) [3–8]. Among the AM technologies, direct laser deposition (DLD) shows outstanding results in manufacturing components at small or large scales, as well as in repairing parts. DLD uses a high energy focused laser beam that melts blown powder flowing through a nozzle. Therefore, the designed component is manufactured by melting the powder layer-by-layer. DLD has advantages over selective laser melting (SLM), including a high deposition rate and faster production, thanks to technological features such as a bigger laser spot size and the ability to deposit thicker layers [9,10].

Several studies have highlighted that the nickel superalloys (e.g., IN718, CM247LC) manufactured by AM are generally crack susceptible; therefore, it is fundamental to understand the effect of the process parameters and their combinations to avoid triggering the phenomena that may promote crack formation [11–13]. Generally, the formation and propagation of cracks in the AM of CM247LC is an issue not only during the manufacturing step, but also during the subsequent heat treatment (post-weld heat treatment; PWHT) or during the service. Crack formation mechanisms can be broadly classed into four main typologies.

- Solidification cracking

This type of crack usually occurs within the melt pool (mushy zone) where the material in not fully solidified (partial solid state). Cracks form when the temperature drops below the coherence temperature; the formation of the dendrites follows the heat source direction toward the liquid phase in the interdendritic regions. The residual liquid phase acts as stress raiser and crack initiator and the relatively weak solid–liquid boundaries separate to create an intergranular rupture. This type of cracking is also known as hot-tearing [14–17].

- Liquation cracking

This usually happens in the heat affected zone (HAZ) where the bulk material is heated rapidly to a temperature that is lower than the overall liquidus of the material [17]. Generally, the rapid heating due to the welding operation leads to the dissolution of certain grain boundary phases (e.g., γ-γ' in Ni superalloys) and other metallurgical phases such as carbides that are characterised by lower melting temperatures. Therefore, these liquid films between the grain boundaries potentially act as crack initiation points during welding in combination with the residual stresses [18–21].

- Strain Age Cracking (SAC)

This type of crack mainly occurs in γ' precipitate strengthened alloys during PWHT within the ageing region either as part of stress relief or during the ramp phase of a solution treatment or high temperature service [14]. Repeated reheating during AM because of the layer-by-layer melting technique can also cause this form of cracking. During the ageing process the Al and Ti contribute to forming the γ' strengthening phase and the material increases its strength whilst reducing ductility; therefore, the residual stress and the induced stress from the precipitation of the γ' result in internal strain that exceeds the limited ductility of the material leading to crack formation, usually at the grain boundaries [15,18].

- Ductility-dip cracking (DDC)

This kind of crack occurs due to a reduction in ductility (referred to as severe ductility drop) within a certain temperature range below the solidus temperature, and usually occurs along the grain boundaries [22]. This is due to a combination of the macroscopic thermal and solidification stresses generated at elevated temperatures, and the microscopic stresses generated within the grain boundaries due to the precipitation of partially coherent carbide phases. High chromium nickel superalloys, while resistant to corrosion and stress corrosion cracking, are known to be particularly susceptible to DDC [23,24]. The majority of CM247LC literature related to DLD refers to cracking issues. CM247LC is more susceptible to cracking than other nickel-based superalloys, such as IN718 and IN738, due to the higher γ' fraction or slower precipitating γ'' phase [25–27].

This article proposes an alternative technique to manufacture crack-free thin geometries by DLD of CM247LC. The study of the cracks detected in some samples allowed us to understand the reason for crack formation during the deposition leading to the realisation of a process parameter map that shows the crack-free operative area. Moreover, CM247LC requires heat treatment like other Ni superalloys in order to develop the strengthening phase and to improve the mechanical properties. Therefore, conventional heat treatments and their effects on crack formation were also investigated. Finally, the mechanical property characterisation of the samples produced with optimal parameters was carried out. The overall outcomes reported in this article not only highlight the fundamental role of the appropriate process parameters, but also explain how they affect crack formation in combination with heat treatments.

2. Experimental procedure

Thin walls were produced using a TRUMPF TLC 1005 equipped with a 4 kW diode laser (Trumpf TrueDisk 4002) and a three-beam nozzle. During the deposition, the laser beam focused to a spot size of 1.4 mm and the standoff distance (distance between the substrate and the laser head) was set to 10 mm. For each test, an IN718 substrate, preliminarily sanded and cleaned with ethanol to remove any contamination, was used to deposit the thin walls Fig. 1. Before each deposition, four pre-heating scan lines were carried out to warm up the surface of the substrate and reduce the

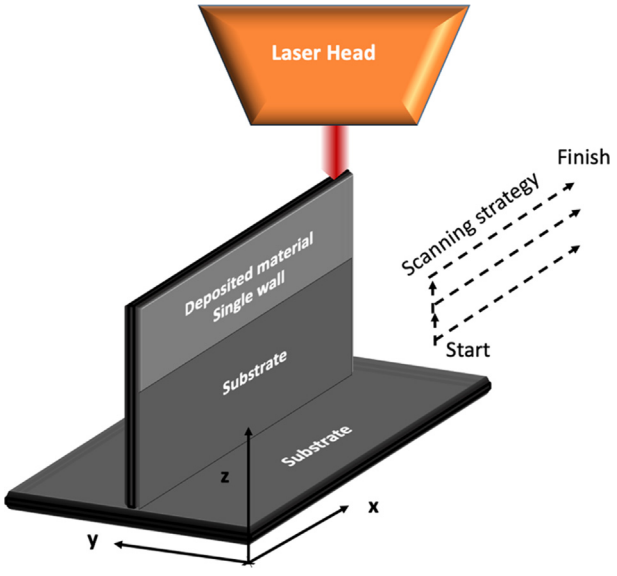

Fig. 1. Schematic illustration of the DLD process; deposition of the thin wall and the scanning strategy.

thermal shock between the substrate and the powder being delivered and melted by the laser head. In contrast with most of the research presented in the literature, this study also investigated the effect of the laser mode, continuous wave (CW) or pulse wave (PW), on the deposition process and its ability to produce crack-free thin geometries. The three-beam nozzle provided a constant powder flow rate of 25 g/min, while a defocusing of the powder stream (powder stream focus was below the substrate) was set at 2 mm. The powder and laser defocusing values were selected in order to compensate for any lack of deposition due to the uneven horizontal surface of the walls. An inert environment was created by filling the building volume with argon, and the oxygen level during deposition was always lower than 300 ppm. A pre-heating scan with the laser (no powder was delivered during this step) was conducted to reduce the accumulation of residual stresses during the build process and reduce the risk of delamination between the deposited wall and the substrate. In detail, the laser was moving along the established deposition path (linear path 45 mm length) at a constant speed (800 mm/min). The pre-heating strategy was characterised by moving the laser source twice along the linear path without switching off the laser. Although the literature reports works in which the pre-heated bed was used to mitigate the residual stress effect and reduce the cooling rate, in this study the local pre-heating by the laser was considered to be effective in reducing the residual stress. Indeed, a local pre-heating by the laser offers several advantages, such as a simplified experimental set-up (no heat bed is required) and can also be applied when repairing components, however, no record of the actual pre-heat temperature was collected. Regarding the two types of laser mode, CW was characterised by having the same average and peak power during the deposition, while PW was represented by a modulated square wave with a 50% duty cycle and frequency of 80 Hz. Although, the PW maximum power was equal to the CW maximum power, the minimum power was set at 2% of the maximum power. A similar approach was used in another work and has been reported by Stano et al. [28].

The process parameter details are listed in Table 1. Multiple single walls with lengths of 45 mm and heights of 20 mm were produced. Subsequently, further thin walls of 90 mm in length and 20 mm in height were produced to extract tensile specimens for mechanical property characterisation. The walls were deposited at different power values (300, 400, 600 and 800 W), different laser modes (CW, PW) and different scanning speeds (300, 500 and 700 mm/min). It is important to highlight that during the deposition of the walls using the CW laser mode, only the process parameters characterised by laser power of 300 W with scanning speeds of 300, 500, 700 mm/min, and laser power of 400 W with a scanning speed of 700 mm/min allowed thin walls to be built without macro-cracks. The use of CW with laser powers of 600 and 800 W with scanning speeds between 300 and 700 mm/min, and laser power of 400 W with scanning speeds of 300 and 500 mm/min were not considered in the analyses owing to the significant amount of cracking that appeared after the deposition process.

The heat input or energy density (J/mm) related to the CW mode can be defined as shown in Eq. (1) [29], in which P represents the power while V is the scanning speed of the laser head.

$$Heat\ \ input = P/V \tag{1}$$

Eq. (2) was used to estimate the weighted average power (WAP) used during deposition using the PW laser mode. P_{max} is the maximum power, P_{min} is 2% of the maximum power, and t_{min} and t_{max} are both equal to 50% since the pulse shape is symmetric.

$$\mathrm{WAP} = P_{max}\left(\frac{t_{max}}{100}\right) + P_{min}\left(\frac{t_{min}}{100}\right) \tag{2}$$

Finally, Eqs. (1) and (2) were combined to estimate the energy density when the PW mode was used (Eq. (3)).

$$Heat\ \ input = \left[P_{max}\left(\frac{t_{max}}{100}\right) + P_{min}\left(\frac{t_{min}}{100}\right)\right]/V \tag{3}$$

During the deposition process, an infrared (IR) camera was used to monitor the thermal field distribution. The scanning strategy was unidirectional: the laser moved along the x axis for 90 mm (first layer), the laser was switched off then moved rapidly in the z direction by the specific height of the layer thickness, and then moved back along the x direction by 90 mm; then the laser was switched on again to deposit the second layer.

The CM247LC powder with particles ranging from 53 to 180 μm was analysed using scanning electron microscopy (SEM). The produced samples that did not show particular defects (e.g., excessive porosity, solidification cracks) were heat treated. The successfully manufactured walls were cut (in the build direction) by the EDM (electro discharge machine). The test was performed using a Zwick Roell 1484 universal testing machine, using an extensometer with a gauge length of 20 mm. All the specimens were simultaneously surface ground to ensure identical surface quality. Fig. 2 shows the tensile specimen cut orientation from the wall specimens were obtained to assess the mechanical properties after the heat treatments. The surfaces of the tensile specimens were ground and polished to reduce the effect of the surface roughness on the mechanical properties. The walls were also cut and metallographically prepared in order to evaluate the microstructure by SEM,

Table 1
Process parameters and energy density.

Sample	Laser mode	Peak power	Power 2%	Scanning speed		t_{max}/t_{min}	WAP	Heat input
		(W)		(mm/min)	(mm/sec)	ratio	(W)	(J/mm)
CW300/700	CW	300	–	700	11.67	–	300	25.71
CW300/300	CW	300	–	300	5.00	–	300	60.00
CW300/500	CW	300	–	500	8.33	–	300	36.00
CW400/700	CW	400	–	700	11.67	–	400	34.29
PW300/300	PW	300	6	300	5.00	50	153	30.60
PW300/500	PW	300	6	500	8.33	50	153	18.36
PW300/700	PW	300	6	700	11.67	50	153	13.11
PW400/300	PW	400	8	300	5.00	50	204	40.80
PW400/500	PW	400	8	500	8.33	50	204	24.48
PW400/700	PW	400	8	700	11.67	50	204	17.49
PW600/300	PW	600	12	300	5.00	50	306	61.20
PW600/500	PW	600	12	500	8.33	50	306	36.72
PW600/700	PW	600	12	700	11.67	50	306	26.23
PW800/300	PW	800	16	300	5.00	50	408	81.60
PW800/500	PW	800	16	500	8.33	50	408	48.96
PW800/700	PW	800	16	700	11.67	50	408	34.97

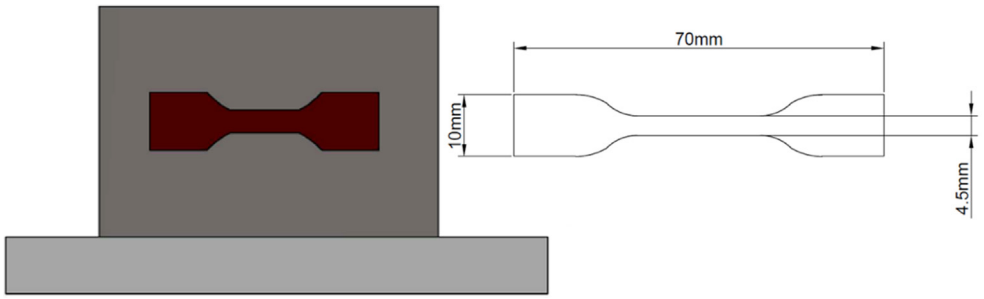

Fig. 2. Schematic drawing of the extraction of the samples by EDM, geometry and sample dimensions.

electron backscattered diffraction (EBSD) and energy dispersive X-ray spectroscopy (EDX). Moreover, X-ray diffraction (XRD) analyses were carried out to evaluate the presence of the different phases. The SEM images were analysed by ImageJ processing software by Fiji to characterise the cracks and to evaluate the porosity.

3. Results and discussion

3.1. Powder characterisation

The metal powder used in this work was argon gas atomised CM247LC (53–180 μm) with almost no satellite formation, supplied by Sandvik Osprey Ltd. Fig. 2 shows the cross sections of CM247LC powder particles analysed by backscattered SEM. The powder was hot mounted within resin and the sample was ground, polished and electro-etched to reveal the microstructure. The results show that the powder was predominantly spherical with limited satellites, while the microstructure was near fully dense with an equiaxed grain structure characterised by submicron precipitates. Chemical composition analysis was performed by Exova [30] using inductively coupled plasma optical emission spectrometry and the results are provided in Table 2.

The SEM micrographs of CM247LC cross sectioned powder particles show the fine cellular grain structure and evidence of carbide formation between the cell boundaries. The dendritic structure is also evident [Fig. 2(b) and (c)] although it is very limited. The very fine white particles located in the interdendritic regions are likely to be Hf or Ta, since this is found to vary the most when conducting EDX.

3.2. Effect of the process parameters on defect and crack formation

Different process parameters and laser operative modes (CW and PW) led to the production of thin walls with several types of defects (e.g., pores, micro- and/or macro-cracks) as well as crack-free thin walls that had been successfully manufactured. It is important to point out that the type of cracks observed via SEM after the deposition originated and propagated along the grain boundaries, as highlighted in Fig. 3. The SEM analysis of the longitudinal and cross section of each wall allowed us to define the map of the process parameter effects to establish the crack-free domain (Fig. 3). In particular, the process parameter map was populated using the SEM analysis of the samples to allow an easy comparison of the defects depending on the scan speed, power and laser operative mode. The entire surface of the map was divided into three separate regions, as shown in Fig. 4. In general, the areas enclosed by the red circle and rectangle are characterised by process parameters that allowed the building of thin walls without visible cracks, but the presence of cracks (micro-scale or extended) as well as pores and lack of fusion were revealed by SEM analyses. Within the green area, the process parameters used led to the manufacture of thin walls with limited pores (PW only).

3.2.1. Red circle zone (low scanning speed and low power)

As previously mentioned, the red circled region combines the process parameters and laser operative modes that manufactured thin walls containing cracks, pores and lack of fusion. In detail (Fig. 5), PW300/300 had small to medium pores, lack of fusion and micro-cracks, whereas PW400/300 had small to medium pores, no lack of fusion but still some micro-cracks. Comparing PW300/300 with PW400/300, an increase in power led to more micro-cracks and a decrease in pore numbers avoiding lack of fusion. The WAP (153 W, 204 W) combined with a low scanning speed (300 mm/min) resulted in the formation of cracks. Compared with PW400/300, PW600/300 showed a reduction in crack number and severity. CW300/300 had small to medium pores, no lack of fusion, and micro or macro-cracks. Compared with PW600/300, PW600/500 had a macro-crack in the bulk, but no significant differences in pore size and numbers. PW300/500 had small to medium pores, as well as a few large pores, no lack of fusion and one observable micro-crack. Compared with PW300/300, the increase in the scanning speed eliminated some of the stress, which resulted in a reduced number of cracks. PW400/500 had small to medium pores and a few large pores, small lack of fusion in bulk (approximately 40 μm) and one observable micro-crack. PW600/500 had small to medium pores and a few large pores, no lack of fusion and one observable micro-crack. CW600/500 had very small pores, small lack of fusion and visible cracks. PW600/500 showed no lack of fusion when compared with PW400/500 and very similar characteristics when compared with PW300/500. When comparing PW600/300 with PW600/500, the increase in the scanning speed while keeping the power constant resulted in an increase in the pore size, but a decrease in crack numbers.

Table 2
The chemical compositions of CM247LC powder.

Element	Ni	W	Co	Cr	Al	Ta	Hf
wt%	Bal.	9.34	8.73	8.29	5.55	3.11	1.23
Element	**Ti**	**Mo**	**Si**	**Fe**	**C**	**Nb**	**O**
wt%	0.71	0.52	0.11	0.08	0.08	0.05	<100 ppm

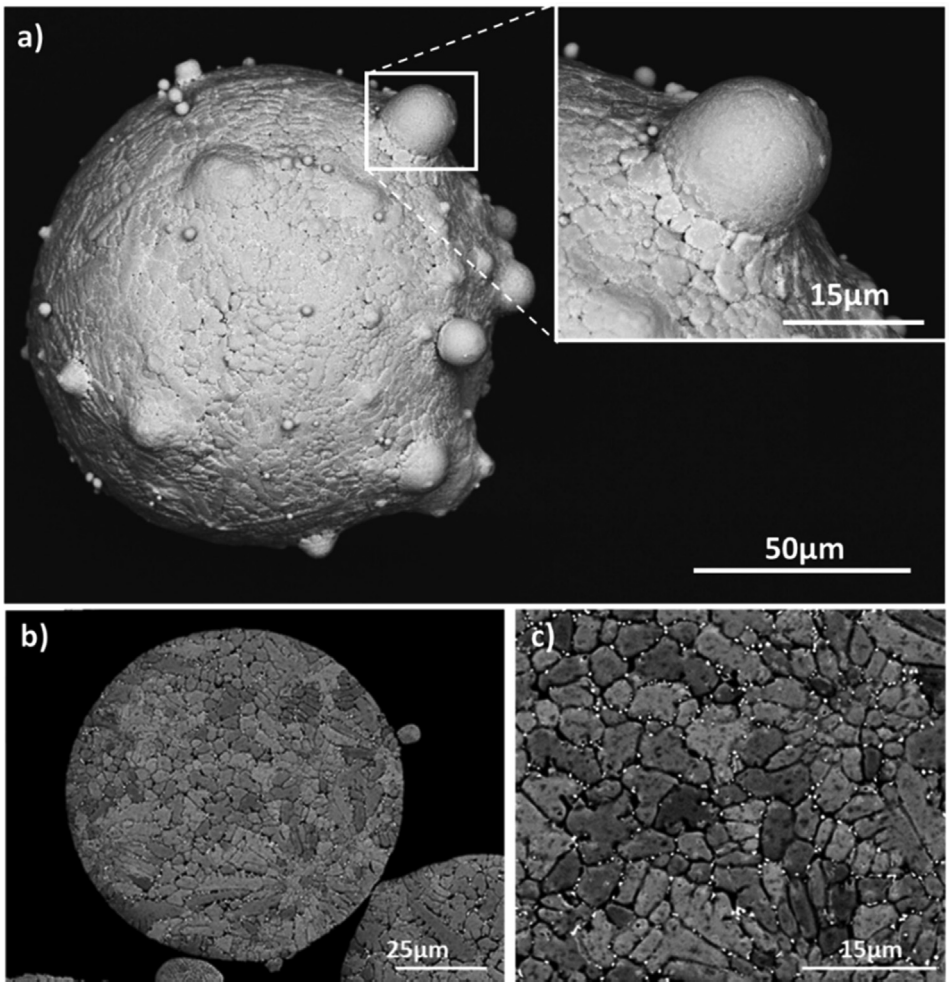

Fig. 3. (a) SEM micrograph of as-received CM247LC powder particles. (b) and (c) SEM micrographs showing cellular particle topography and presence of precipitates on the powder surface.

3.2.2. Red rectangle zone

CW300/700 had small to medium pores, lack of fusion and one observable micro-crack. CW400/700 had small to medium pores, lots of micro-cracks and one macro-crack. PW800/700 had small to large pores, lack of fusion in bulk and no visible cracks. Although, the decrease in power and increase in scanning speed (compared to PW800/500) did not result in stress cracking, it led to a lack of fusion in the bulk material. Moreover, an increase in the size and number of pores was observed. The high power and scanning speed led to stress cracking for samples manufactured via CW, but not for those manufactured via PW (Fig. 6).

3.2.3. Green triangle analysis

PW800/500 had limited small to medium pores, and no lack of fusion or visible cracks were detected. PW600/700 had small to medium pores, and no lack of fusion or visible cracks were observed. The higher power of PW600/700 compared with PW400/700 resulted in a reduced size and number of pores and prevented the lack of fusion. PW800/700 showed small to medium pores, no lack of fusion and no visible cracks. The higher power and scanning speed enabled more gas to be trapped during the deposition and, therefore, the pores were larger. Compared with PW600/700, the pores had increased in size, but decreased in numbers. When comparing PW800/500 with PW800/700, the increase in the scanning speed at a constant power resulted in an increase in the pore size and numbers and no lack of fusion (Fig. 7).

Both CW and PW beams were able to produce consolidated parts; however, all the CW parts showed cracks, some porosity and lack of fusion. On the other hand, some of the parts produced by PW were crack-free, had no lack of fusion and showed very limited porosity, suggesting reliability for manufacturing or repairing components. Therefore, it is clear that the use of the PW mode affects the final properties of the material. Fig. 8 summarises the discontinuities observed in the samples produced using a variety of parameters.

3.3. Solidification cracking during the DLD process

IR imaging was used to detect the cracks formed during the deposition process. Fig. 9 shows the formation of the wall produced by CW at 600 W with a scanning speed of 500 mm/min. Although the crack formation is the most interesting result, it is possible to observe that as the number of layers deposited increases there is an accumulation of heat in the wall, and particularly from the central region up to the top of the wall. This result confirms the role of the substrate in reducing the temperature within the first layers deposited, as it acts as a heat sink. According to Raghavan et al. [31], this leads to more equiaxial than columnar grains in the bottom of the microstructure. During the deposition of the 20th layer a small crack appeared and subsequently more cracks formed and propagated while new layers were deposited. These cracks occurred in the mushy zone where the material was not fully solidified. The cracks

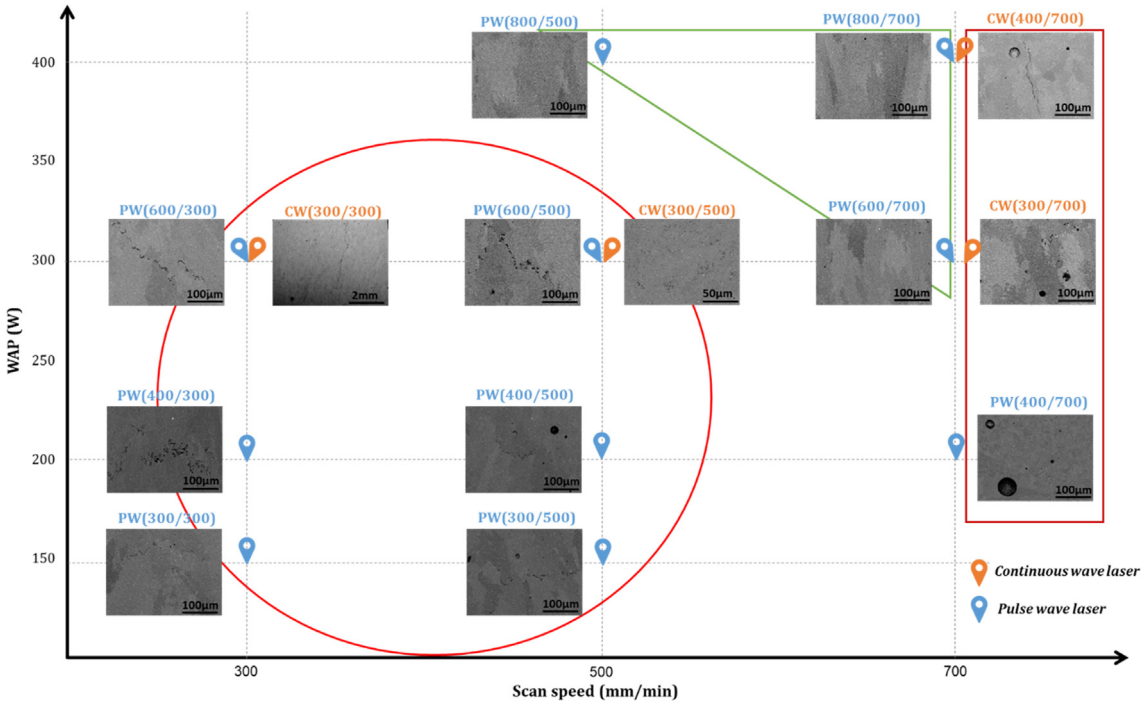

Fig. 4. Comparison in terms of process parameters and resultant microstructural characteristics.

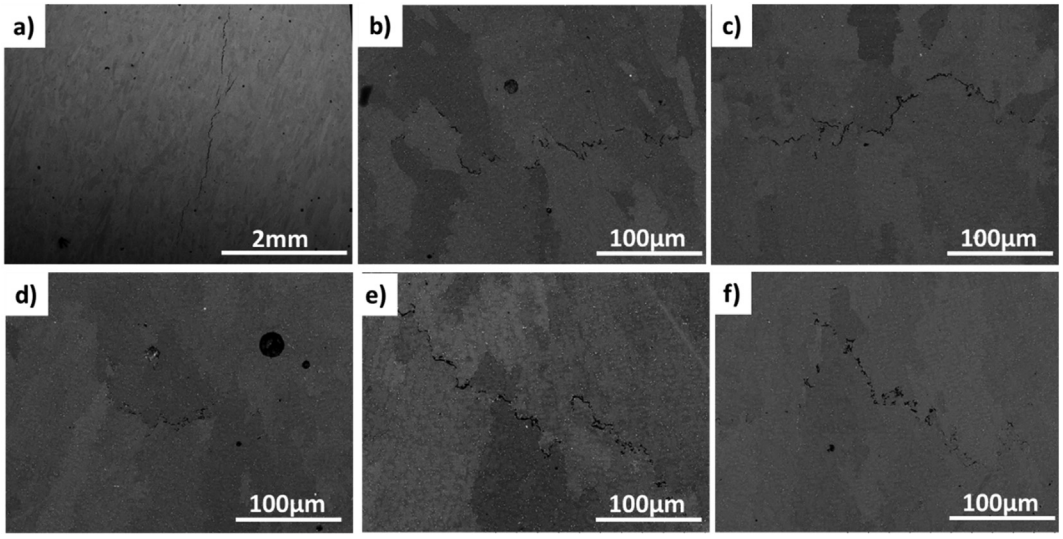

Fig. 5. SEM Pictures of microstructure of the following samples (a) CW300/300, (b) PW300/500, (c) PW400/300, (d) PW400/500, (e) PW600/300, (f) PW600/500.

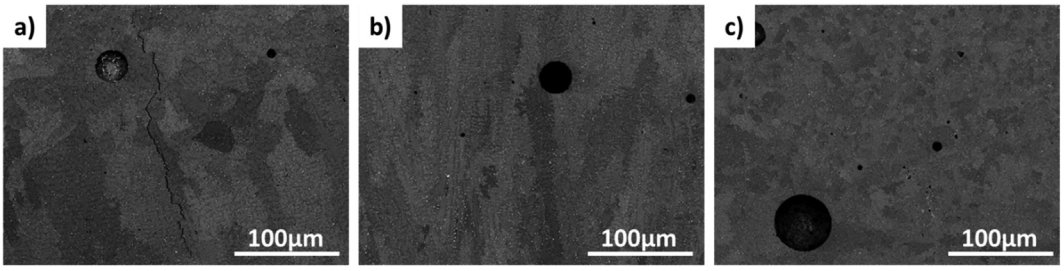

Fig. 6. SEM Pictures of microstructure of the following samples (a) CW400/700, (b) CW300/700, (c) PW400/700.

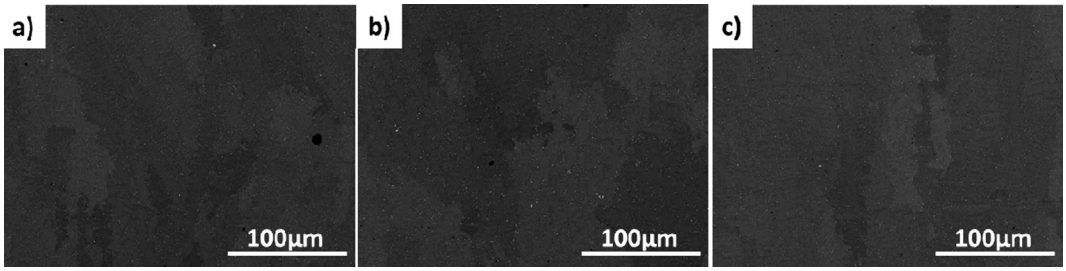

Fig. 7. SEM Pictures of microstructure of the following samples (a) PW600/700, (b) PW800/500, (c) PW800/700.

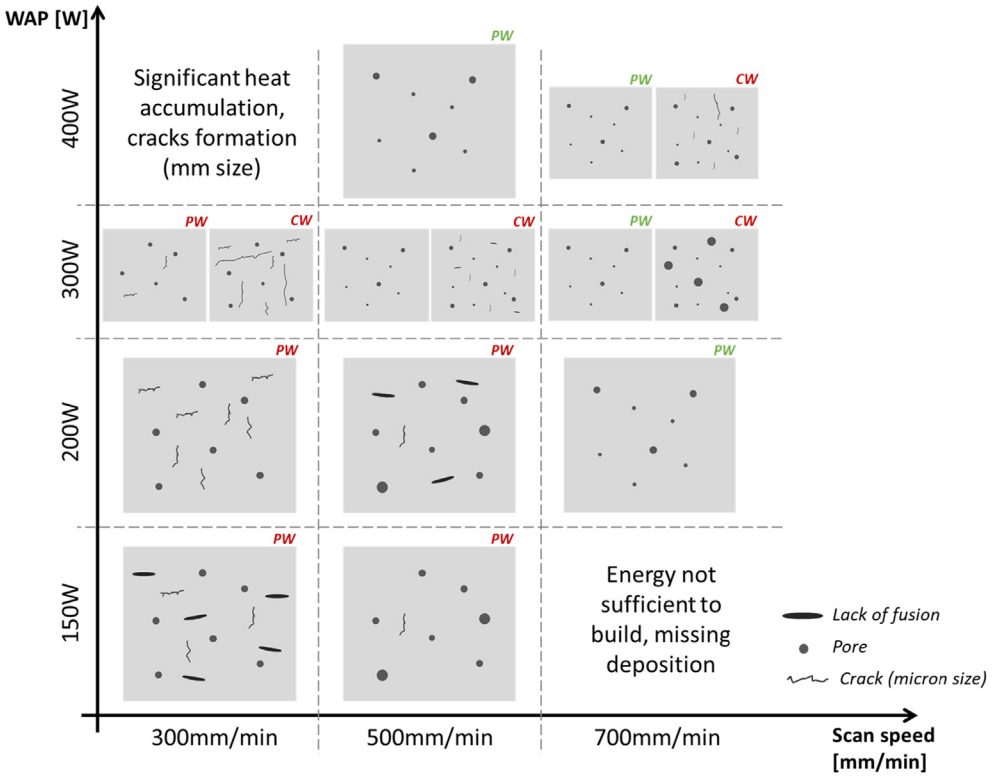

Fig. 8. Summary of samples' discontinuities and resultant microstructural characteristics.

formed when the temperature dropped below the coherence temperature, and the formation of the dendrites followed the direction of the heat source toward the liquid phase in the interdendritic regions. The liquid regions that remained acted as stress concentration and crack initiator sites and the relatively weak solid–liquid boundaries separated to form an intergranular rupture [17]. This result was also confirmed by the SEM analysis; indeed, the main macro-cracks were particularly vertically orientated in the dendritic growth direction and the cracks were nucleated and propagated between the dendrites.

Fig. 10 represents the thermal field distribution during the deposition of the thin wall using the PW laser mode at 800 W with a scanning speed of 500 mm/min. This picture shows immediately that the heat accumulation was lower than that evaluated during the CW laser mode deposition (Fig. 9). The PW laser mode enhanced the cooling rate and consequently lowered the temperature, such that a reduced heat accumulation characterised the entire deposition process. Moreover, no macro-cracks were detected, highlighting the benefit of using the PW to avoid failures in the manufacturing process. Finally, the PW showed a significant advantage in producing crack-free thin components with CM247LC.

3.4. Strain Age Cracking (SAC) during the heat treatment

Heat treatment was carried out on the samples that had been successfully produced without any cracks (micro- or macro-cracks). However, one sample that showed some solidification cracks was also included in the treatment to evaluate its effect on the SAC susceptibility of the sample. A double ageing heat treatment was performed on the samples: 980 °C for 5 h followed by furnace cooling to 870 °C for 20 h followed by furnace cooling to room temperature. The ageing process increases the material's strength while reducing its ductility. Fig. 11 shows a thin wall characterised by solidification cracks before and after heat treatment. It is possible to observe that new cracks appeared and these can be classified as SAC; in this case, the carbides acted as stress riser or crack initiation sites. Moreover, the residual stress and the induced stress due to the precipitation of the γ' resulted in strain that exceeded the limited ductility of the material and

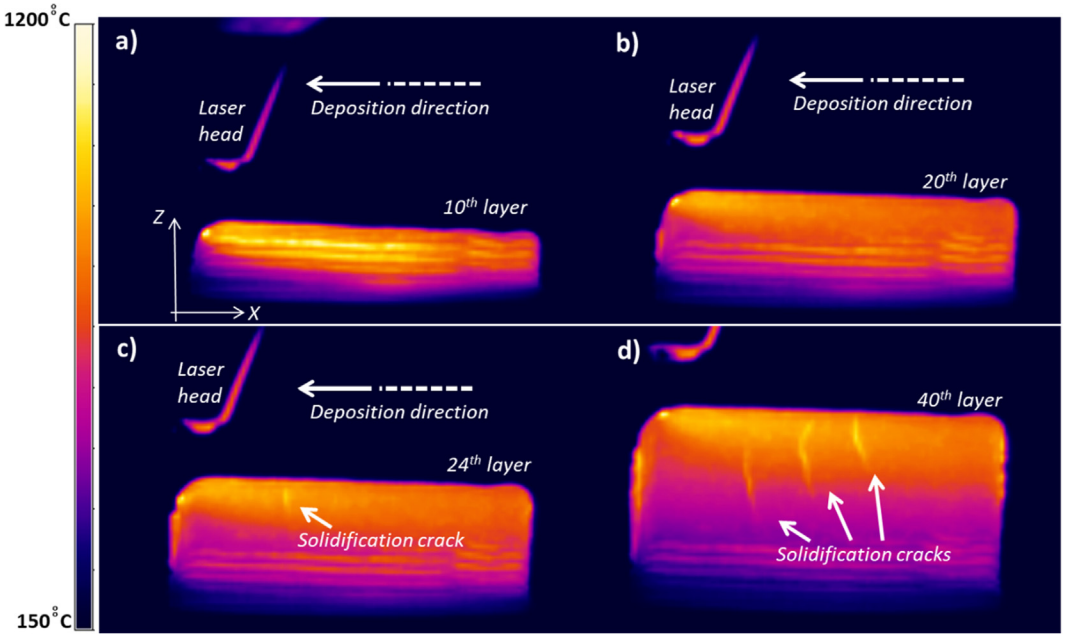

Fig. 9. Thermal field distribution on the z-x plane of the CW600/500 deposited walls showing crack formation by layer.

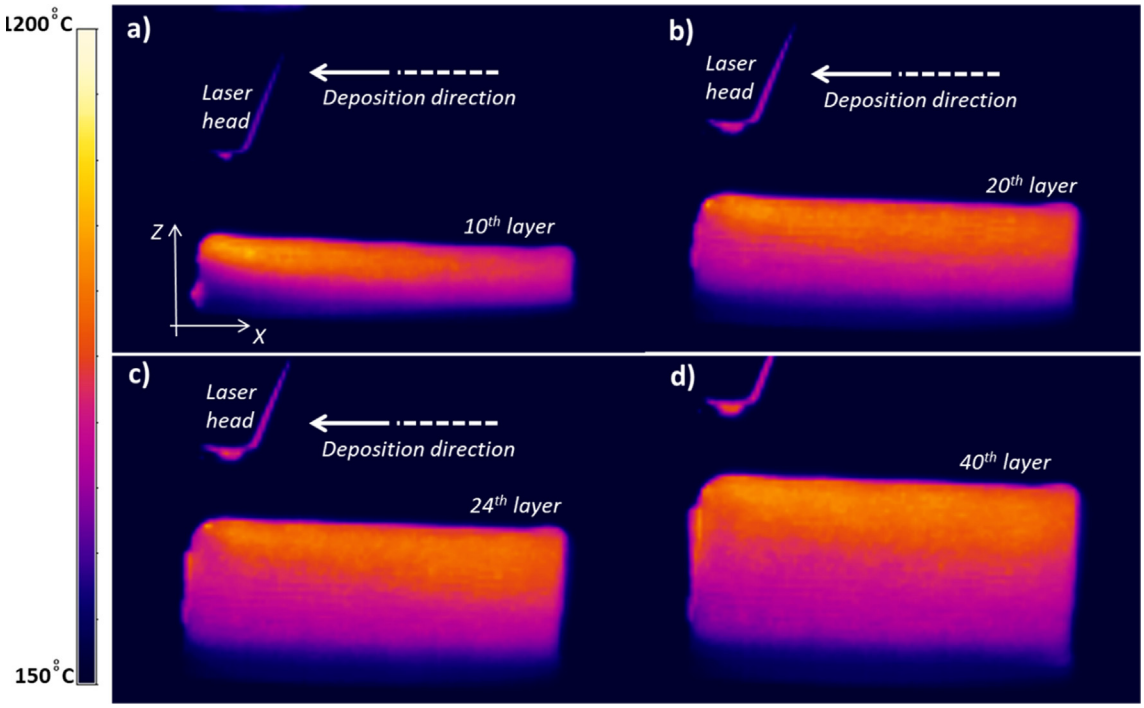

Fig. 10. Thermal field distribution on the z-x plane of the PW800W/500 deposited wall showing no cracks.

provoked the formation of cracks, usually at the grain boundaries. Fig. 12 shows one of the thin walls successfully produced without cracks. It is possible to observe that the heat treatment did not affect the part in terms of crack formation; therefore, the process parameters used during the DLD process produced a component with a very low SAC susceptibility.

In particular, the three samples produced by the PW laser that were in the green triangle (no cracks, no lack of fusion and small porosity) passed the ageing post heat treatment with no visible defects, except the sample PW800/500, in which a small horizontal crack appeared immediately after heat treatment [Fig. 12(b)].

3.5. Microstructure and chemical composition

Fig. 13 shows the microstructure observed by BSE microscopy on the cross section of the sample PW800/500 before heat treatment. The peculiar microstructure usually observed on Ni-superalloy parts produced by DLD is also noted in this study. The elongated columnar dendritic microstructure was developed through the build direction (z) and the orientation was due to the heat source movement [Fig. 13(a)]. The use of the secondary electron detector allowed observation of the γ' formed due to the DLD process. The size as well as the shape of the γ' are clearly com-

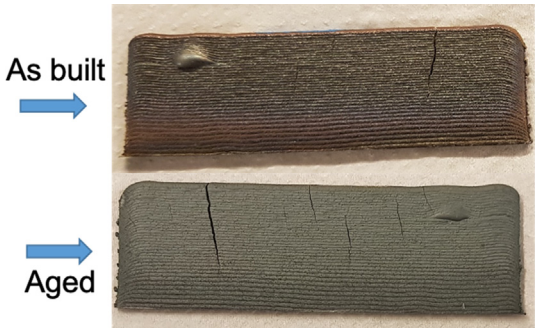

Fig. 11. Failed samples that cracked during deposition, before and after heat treatment.

parable with those observed in the Ni superalloys manufactured by conventional processes and heat treated. The strengthening phase formed was characterised by a spherical shape with a submicron size [Fig. 13(d) and (e)].

The interdendritic region was characterised by submicron precipitates [white colour represented in the BSE Fig. 13(c)]. EDX measurements were carried out to confirm the chemical elements of the precipitates. The elemental concentration maps showed that the area surrounding the precipitates was rich in Al, Ti, W, Co, Cr and Ni. The white particles (precipitates) were found to be rich in Hf and Ta and they were the MC carbides. The alloying elements Hf and Ta are known to form MC-type carbides that replace Ni, Cr and Co. Generally, carbides appeared to be 1 μm in size, although a finer type of carbide was also observed more frequently. A homogenous distribution of carbides is necessary for good properties, hence carbide precipitation at grain boundaries can provide grain boundary strengthening via pinning effects, while fine carbides precipitated throughout the matrix can provide dispersion strengthening effects [32] (Fig. 14).

Kikel and Parker [33] stated that crystallographic orientation had an effect on the susceptibility to DDC cracking; the strain threshold for DDC reduced from 2.5% strain to 1% strain in the presence of high angle grain boundaries. The first stages of recovery involve rotations of low angle grain boundaries [34]. Local variations in crystallographic orientation have been identified by Muñoz-Moreno et al. [35]. Therefore, both the increase in DDC cracking and the change in Young's modulus indicate the onset of recovery at lower temperatures.

The EBSD analysis allowed us to distinguish the grains that were difficult to properly detect by SEM analysis, and their orientation has also been revealed. In detail, Fig. 15(a) and (b) show the orientation of the inverse pole figure (IPF) map of the cross section and longitudinal section, respectively, of the sample produced by PW at 800 W with a scanning speed of 700 mm/min. The use of the PW allowed the development of a microstructure with a random texture. The kernel average misorientation map [Fig. 15(c) and (d)] confirm the presence of misorientation angles within grains that are typically lower than 5°, although more isolated regions of higher misorientations were also observed. The xy side (build direction or cross section) and xz side (bulk direction) did not contain dislocation arrays or dislocations recovered deformed, as shown in Fig. 15(c) and (d).

Further metallographic analyses were carried out on the heat-treated samples. In detail, the heat treatment enhanced the dissolution of the γ/γ' and the grain boundaries were more visible with carbides embedded in the γ'. The interior of the grains was characterised by the γ' particles, as shown in Fig. 16. It is worth noting that the shape and the size changed due to the heat treatment. The particles were initially more spherical [Fig. 13(d)], and after the heat treatment they started to assume a more cuboidal appearance, although this was not fully developed [Fig. 16(c)]. Usually, CM247LC γ' particles look like split cubes after solution treatment and ageing; however, in this study only ageing (870 °C for 20 h) without a previous solution treatment was performed. Therefore, the temperature of the ageing treatment and the duration were not high enough to form the cube-type primary γ' with size usually close to 1 μm, as reported by [30]. It is important to highlight that the coarse γ' particles at the grain boundaries can help to pin the grains. Furthermore, the irregular morphology of the grain boundaries, which arises due to particles pinning the boundary, can help to inhibit grain boundary sliding. In this case, the resultant γ', although not fully developed into the cube-like shape, was coarser and denser than the one observed in the as deposited samples.

The microstructure after the ageing treatment was more irregular in its morphology, especially regarding the grain boundaries, which could potentially inhibit grain boundary sliding. According with the results reported in [30], the grain boundaries were characterised by a necklace structure and the γ' observed in the as-deposited and the heat-treated samples resulted in an ultra-fine γ' that generally appeared within the channels between the cuboidal γ'. Therefore, the high temperature during the deposition process allowed the formation of the γ' but the drastic cooling rate forced the strengthening phase to reach the nanometre scale. Although the long exposure to high temperatures during the heat treatment promoted the growth of the γ', its size was still submicron; therefore, it is still considered to be ultra-fine γ'.

3.6. Texture and phases of the CM247LC: XRD analysis

The results of the powder XRD analysis showed major peaks corresponding to (1 1 1), (2 0 0), (2 2 0) and (3 1 1) with no other minor peaks. Moreover, the XRD patterns for CW and PW samples in the cross section direction (xz) show additional peaks that did not exist on the as-supplied powder. Small peaks appeared at $\theta = 55°$ and 75° for all AM samples regardless of the power mode or the post-processing because the lattice parameter was decreased by depletion of the matrix due to the precipitate and the Laves phase.

The samples shifted by a couple of degrees for the peaks on the (1 1 1) γ compared with the powder. For both power modes the bulk orientation (yz) showed a higher intensity in the preferred

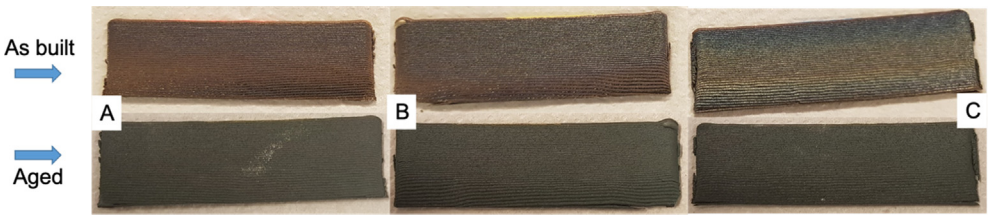

Fig. 12. Green triangle samples before and after heat treatment: (A) PW600/700, (B) PW800/500, (C) PW800/700. (For interpretation of the references to colour in this figure legend, the reader is referred to the web version of this article.)

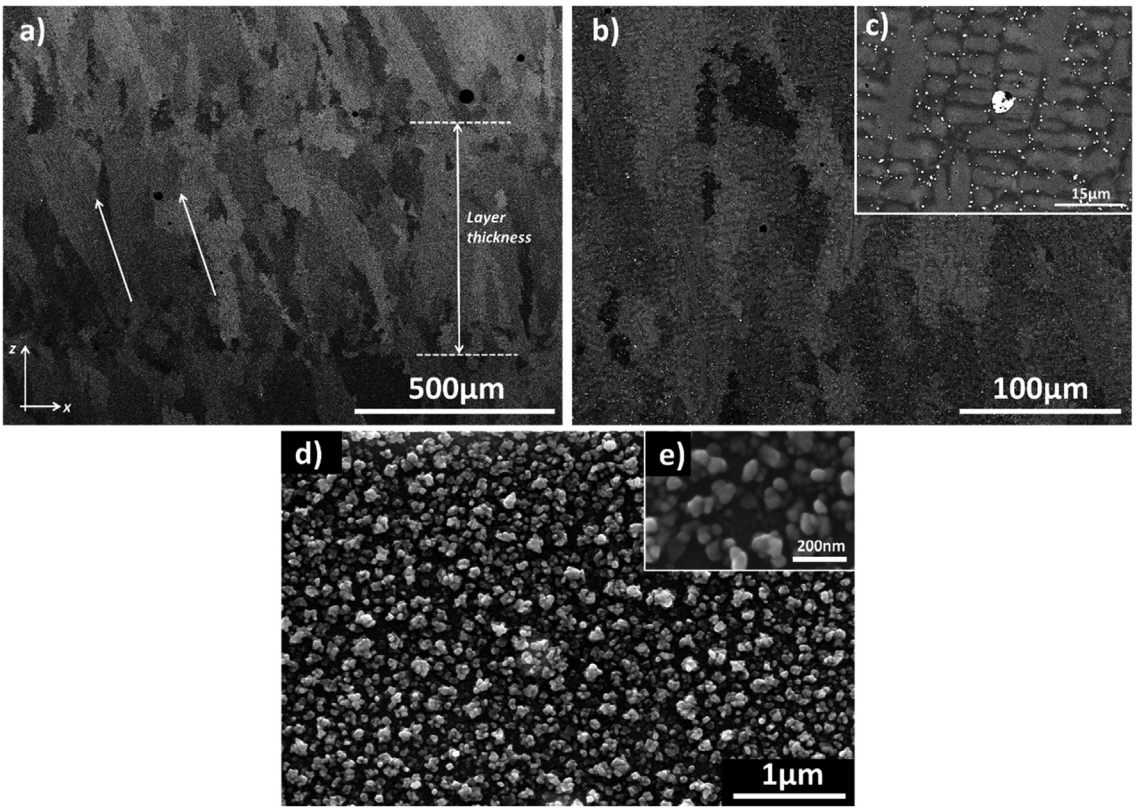

Fig. 13. Microstructure of the as-deposited PW800/500 sample; (a) zx side of the sample, (b) and (c) details of the interdendritic region; (d) and (e) precipitation strengthening phase γ'.

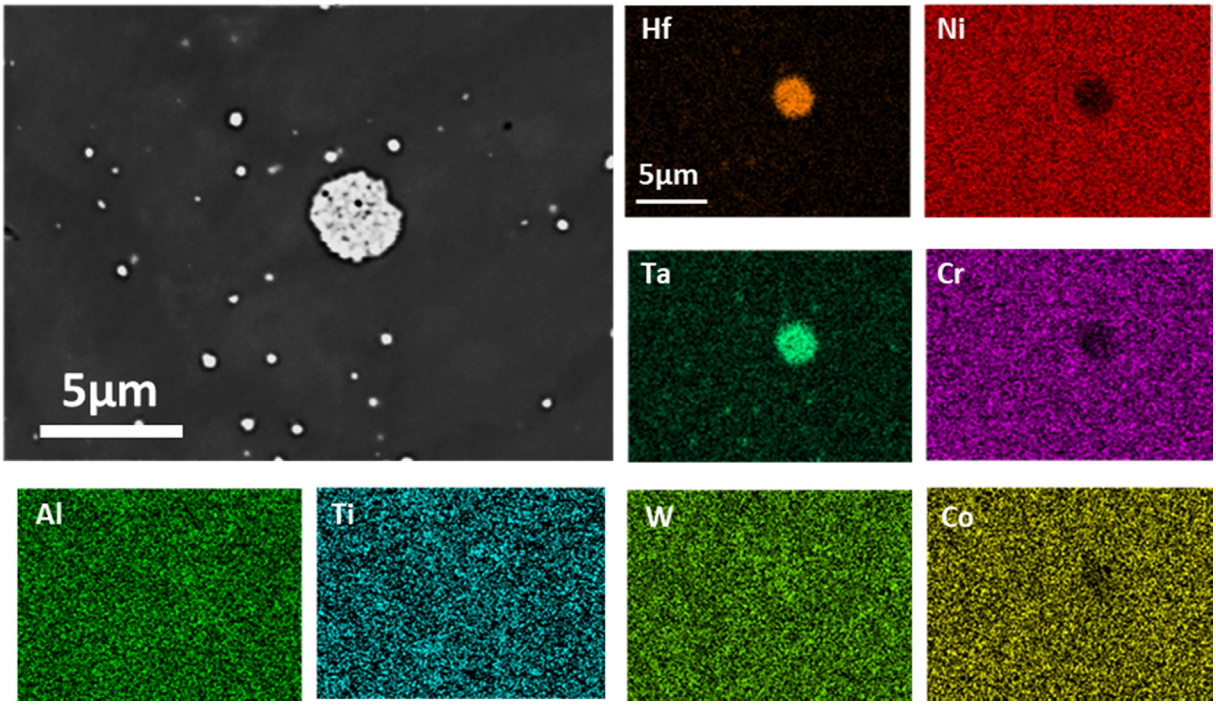

Fig. 14. EDX images of the segregations detected within the interdendritic region.

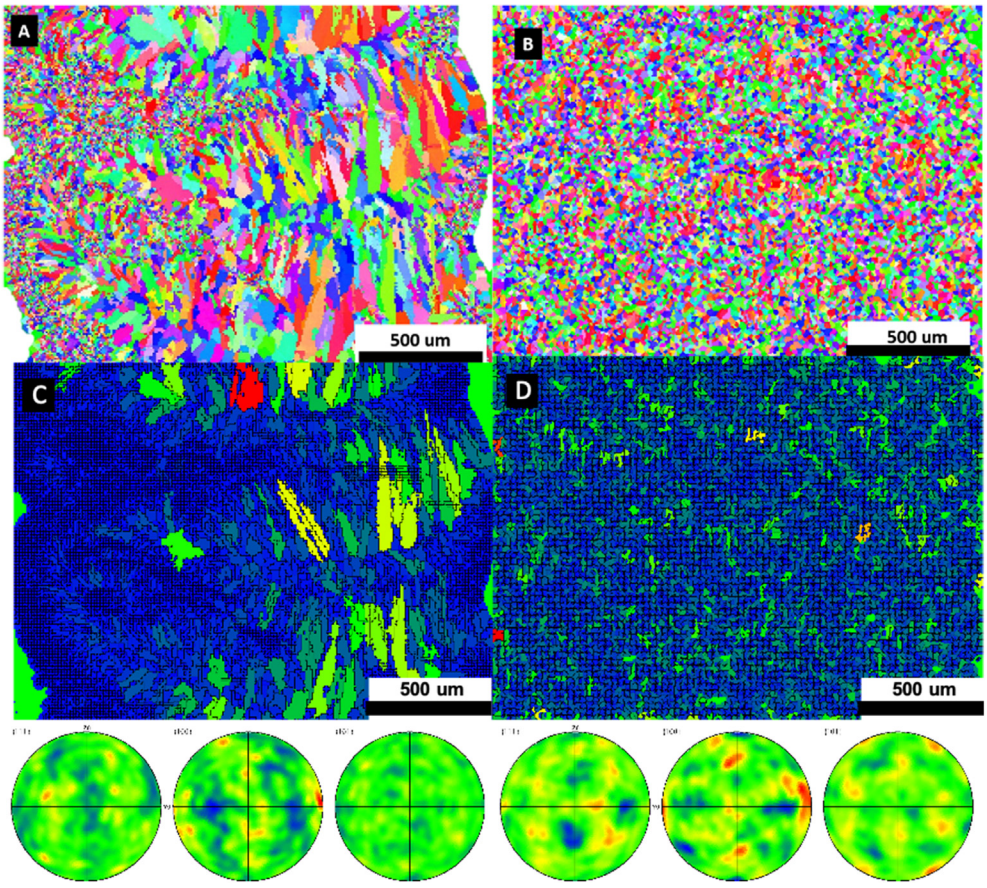

Fig. 15. EBSD of CM247LC samples produced with PW at 800 W and 700 mm/min. IPF map (A) xy, the build direction and (B) xz, the side direction. Kernel average misorientation map (C) xy, the build direction and (D) xz, the side direction.

orientation (2 0 0). Moreover, CW showed a higher intensity in the (2 2 0) and (3 1 1) peaks in the yz direction (Fig. 17).

3.7. Mechanical properties and hardness analysis

The mechanical properties were evaluated through microhardness measurements and tensile tests at room temperature. The hardness analysis was carried out on the three successful builds that were crack free after deposition and heat treatment (PW600/700, PW800/500 and PW800/700). The measurements were carried out on the as-deposited and aged samples. It is obvious that the heat-treated samples showed a higher hardness compared with the as-deposited condition. The results show that the as-deposited samples showed the lowest hardness with values slightly less than 450 HV. The heat treatment increased hardness; almost 100 HV more was measured on each sample compared with the as-deposited condition. The measured hardness of the PW600/700 and PW800/500 samples was almost comparable. It is interesting to note that the increase of the power from 600 W to 800 W while the scan speed was kept at 700 mm/min led to a slight increase in hardness. The increase was also observed when comparing the post heat-treated samples. This increase could be related to the higher heat that the sample experienced during the deposition leading to a slightly higher formation of the strengthening phase. These results are consistent with the trend suggested by the literature. Indeed McNutt [36], who used DLD to perform CM247LC cladding, reported that the hardness increased after performing hot isostatic pressing (HIP) on the manufactured parts. In particular, the hardness was measured in the HAZ from the centre of the deposit to the peripheral region and the variation was from 299 HV to 408 HV, respectively. Yuanbo et al. [37] measured the hardness of a heat-treated sample processed by SLM and the results showed an average value of 455 HV (Fig. 18).

Mechanical tests were performed on the heat-treated samples. The engineering tensile test curves of the CM247LC alloy in the ageing conditions are shown in Fig. 19. A wide comparison with what was already reported in literature was carried out in order to understand the impact of DLD on the mechanical performance in relation to the other near-net-shape manufacturing techniques. Therefore, the mechanical properties reported by Wang et al. [38] after HIP of CM247LC samples produced by SLM and those reported by MacDonald et al. [39] after HIP of CM247LC powder were considered. In particular, Wang et al. [38] measured the ultimate tensile strength at room temperature to be equal to 950 MPa, whereas yield stress was close to 750 MPa while the elongation was approximately 5.5%. MacDonald et al. [39] measured an ultimate tensile strength of 1350 MPa and a yield strength of 815 MPa with an elongation close to 12.7%. It is also important to point out that the powder used in this work was comparable with the one employed by [39]. In this work the highest ultimate tensile strength of 1120 MPa was measured for the PW800/500 sample, followed by the ultimate tensile strength of 1102 MPa for the PW600/700 sample. These results were higher than those reported by Wang et al. [38] for the samples produced by SLM that subsequently underwent HIP; on the other hand, they are smaller than the values reported in [39]. It is interesting to highlight that the yield stress, which in this case was equal to 946 MPa and 795 MPa for PW800/500 and PW600/700, respectively, was comparable with the values reported by Wang et al. [38] and MacDon-

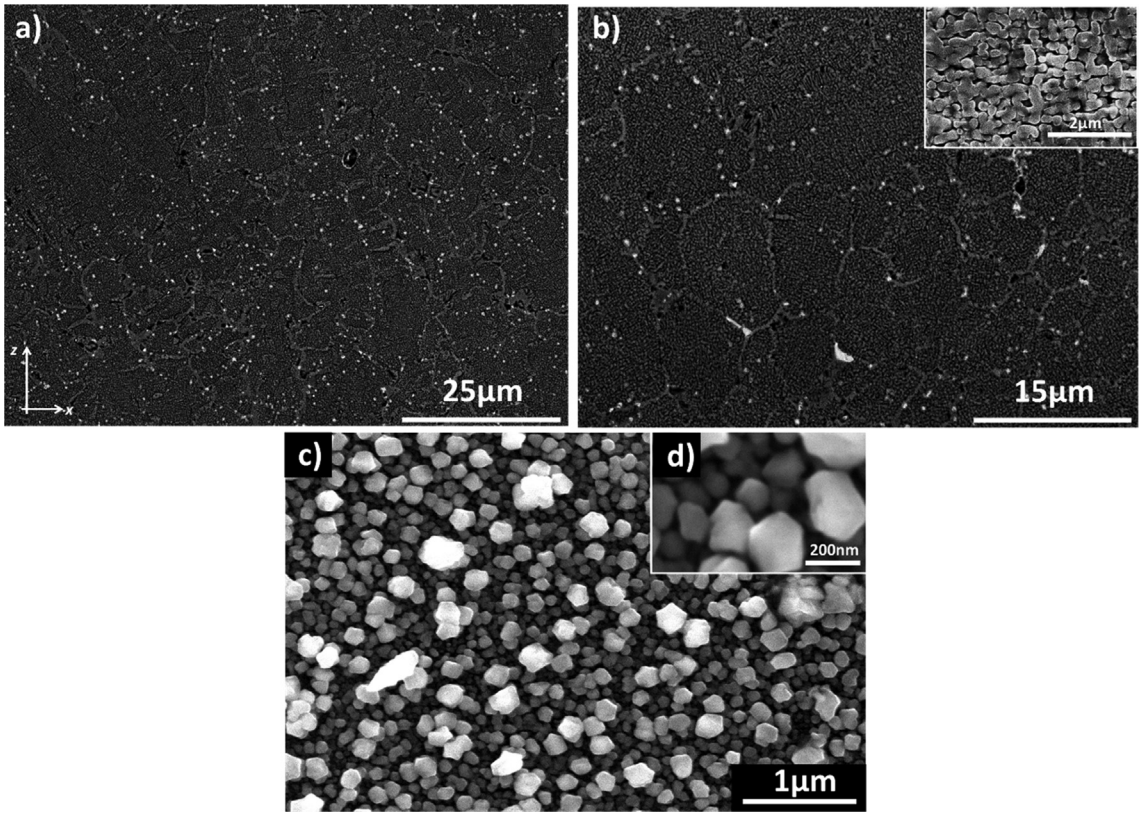

Fig. 16. Microstructure of the heat-treated PW800/500 sample: (a) zx side of the sample, (b) detail of the microstructure; (c) and (d) ultra-fine strengthening phase γ'.

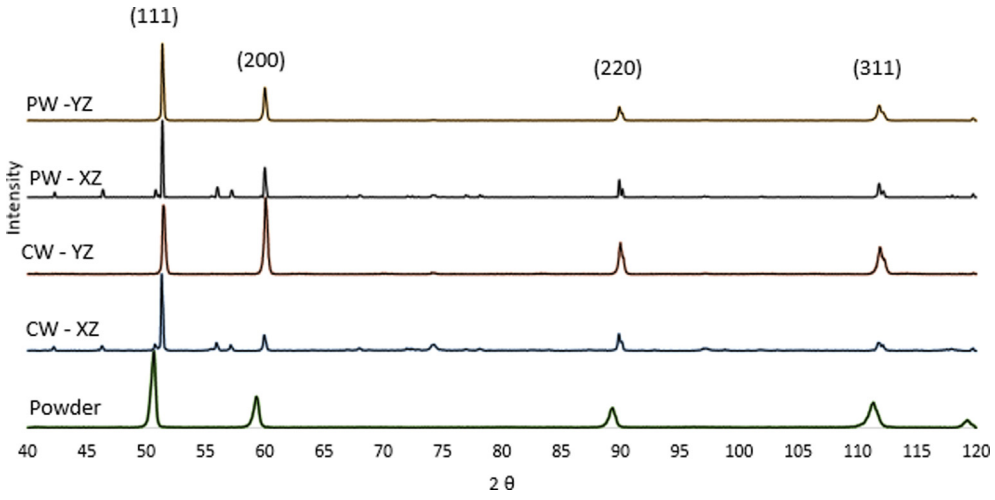

Fig. 17. XRD results of CW and PW, bulk direction and cross section direction.

ald et al. [39]. Finally, the elongation results (1.71–4.32%) were significantly lower than those reported in [39], but still slightly higher than the results of Wang et al. [38]. The details related to the mechanical properties in terms of yield stress, ultimate stress and elongation are listed in Table 3.

The fracture surfaces of the tensile specimens produced with a laser power of 800 W and 600 W with scanning speed of 700 mm/min and the PW laser mode were analysed by SEM as shown in Fig. 20. The characteristics of the surface were revealed through the use of the secondary electron detector [Fig. 20(a)–(e)], while the backscattered detector was used to detect inclusions [Fig. 20(f)]. Considering Fig. 20(a) and (b), the fracture surface was characterised by an irregular shape [Fig. 20(c)] and randomly distributed pores were visible [Fig. 20(e)]. Regardless of the power used to produce the samples, the fracture surface showed similarities: both pores and uneven regions were detected, and the use of

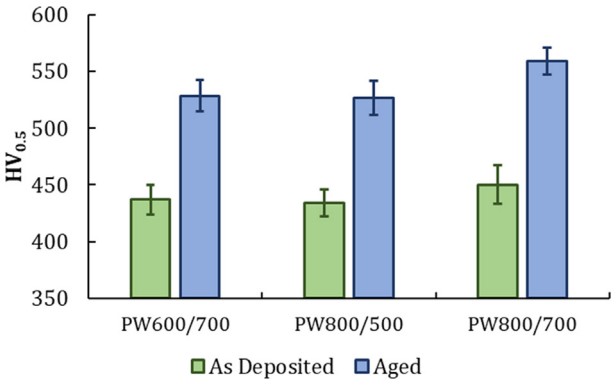

Fig. 18. Hardness results for the CM247LC before and after ageing for various parameters.

Table 3
Tensile strength properties of DLD CM247LC.

Sample	σ_{ys}	σ_{UTS}	e%
PW 600/700	795	1102	4.27
PW 800/700	931	960	1.71
PW 800/500	946	1120	4.32

the backscattered detector highlighted inclusions that were mainly due to the presence of Hf and Ta. The presence of these inclusions that were usually formed between the grain boundaries during the heat treatment (Fig. 16) suggested that the intergranular fracture was the preferred path. Fig. 20(d) shows the presence of microvoid coalescence (dimples). Generally, these types of microvoids nucleate in regions of localised strain discontinuity, usually caused by the presence of inclusions, second phase particles, grain boundaries, etc. [40]. The reduced ductility shown by the PW800/700 sample, compared with the other samples produced with different process parameters could be related to the different percentage of inclusions that could potentially affect the plastic deformation and the formation of the microvoid coalescence.

4. Conclusion

In this research, a process parameters study of DLD processing using CW and PW to produce thin walls made of CM247LC characterised by high density and crack free was performed. The study investigated the reason of the crack formation by monitoring the thermal field during the DLD process. Furthermore, the possibility to perform the heat treatment avoiding further cracks formation (Strain Ageing Cracks) was also assessed and discussed. Finally,

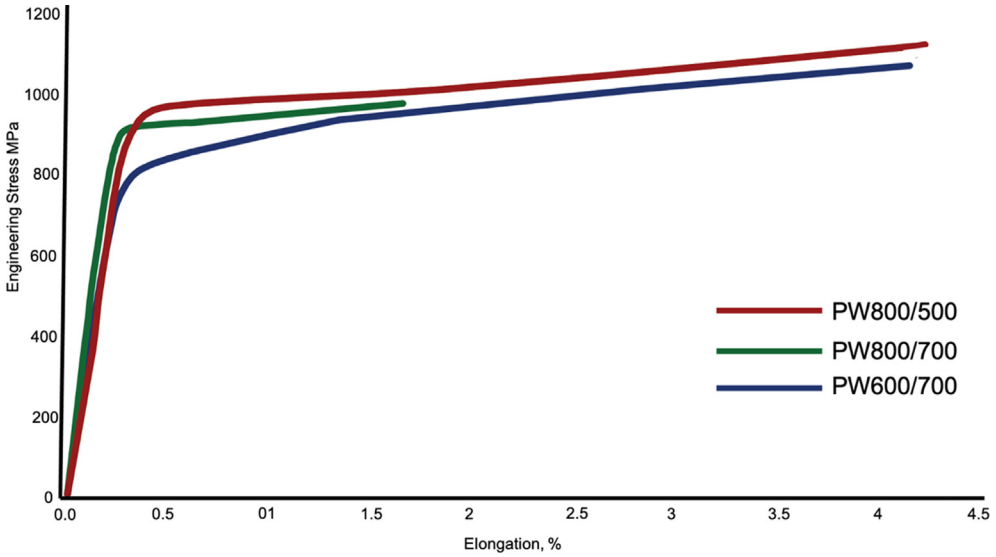

Fig. 19. Engineering stress–strain curves on CM247LC on the ageing condition of the three successful builds.

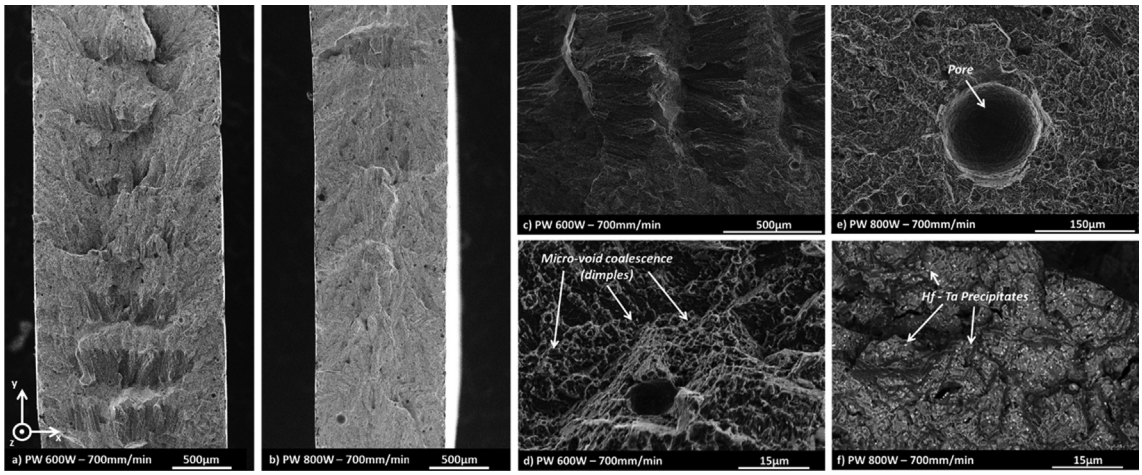

Fig. 20. (a) and (b) cross section of the fracture surfaces; (c) and (d) fracture surface details of the sample produced with laser power of 600 W; (d) and (e) fracture surface details of the sample produced with laser power of 800 W.

the microstructural characterisation and mechanical properties of the thin walls produced with the best combination of process parameters is also reported. The main outcomes produced by this study can be summarised:

- During the DLD process of the CM247LC, different type of defects such as pores, micro and macro cracks were observed, although their presence was depending on the different combination of the process parameters: laser power, laser mode and scan speed.
- Among the different laser power, laser mode and scan speed investigated, a limited window of process parameters characterized by the use of the pulsed wave laser (PW) led to the deposition of crack-free thin walls. In detail, the process parameters characterized by 800 W–500 mm/min, 800 W–700 mm/min and 600 W–700 mm/min allowed to produce crack free thin walls.
- The ageing treatment performed on the samples showed was not long enough to enable the CM247LC alloy to form the cuboidal microstructure. However, it formed ultra-fine γ_t' that usually appears in the channels between the cuboidal γ_p' enhancing the hardness.
- The samples characterised by high residual stressed and cracks induced by the DLD process showed a higher crack density after the heat treatment. This result showed that the combination of the cracks due to the DLD process and the precipitation of the γ' induced by the ageing resulted in the propagation of existing cracks and possibly the formation of new cracks.
- The heat treated thin walls produced with the best process parameters provided higher hardness than the ones DLD + HIP and SLM with full heat treatment observed in literature. While the UTS was comparable with the one reported in literature for samples produced by SLM and HIP, on the other hand the YS was higher, while the elongation was lower. The fracture surface analysis suggests that the material showed a ductile behaviour, although limited elongation was observed from the tensile tests.

Declaration of Competing Interest

The authors declare that they have no known competing financial interests or personal relationships that could have appeared to influence the work reported in this paper.

Acknowledgements

AA would like to acknowledge the funding by the Royal Commission for Jubail and Yanbu (Kingdom of Saudi Arabia) for funding his Ph.D. project. The authors would like to acknowledge the Horizon 2020 research and innovation programme 4DHYBRID "Novel ALL-IN-ONE machines, robots, and systems for affordable, worldwide and lifetime Distributed 3D hybrid manufacturing and repair operations" (Project ID: 723795).

References

[1] R.C. Reed, The Superalloys – Fundamentals and Applications, Cambridge University Press, 2006.
[2] K. Harris, G.L. Erickson, R.E. Schwer, Mar m 247 derivations - CM247LC DS alloy CMSX single crystal alloys properties & performance, Cannon-Muskegon Corporation, pp. 221–230.
[3] K.V. Wong, A. Hernandez, A Review of Additive Manufacturing, Int. Scholarly Res. Netw. 2012 (2012) 10.
[4] J.-P. Kruth, M.C. Leu, T. Nakagawa, Progress in Additive Manufacturing and Rapid Prototyping, Ann. ClRP 47 (2) (1998) 525–540.
[5] G.N. Levy, R. Schindel, J.P. Kruth, K.U. Leuven, Rapid manufacturing and rapid tooling with layer manufacturing (lm) technologies, state of the art and future perspectives, ClRP Ann. (2003) 589–609.
[6] X. Wu, A review of laser fabrication of metallic engineering components and of materials, Mater. Sci. Technol. 23 (6) (2007) 631–640.
[7] X. Wu, J. Mei, Near net shape manufacturing of components using direct laser fabrication technology, J. Mater. Process. Technol. 135 (2-3) (2003) 266–270.
[8] D.D. Gu, W. Meiners, K. Wissenbach, R. Poprawe, Laser additive manufacturing of metallic components: materials, processes and mechanisms, Int. Mater. Rev. 57 (3) (2012) 133–164.
[9] E. Schlienger et al., Near Net shape Production of metal Components using LENS, 1998.
[10] H. Xiao, S.M. Li, W.J. Xiao, Y.Q. Li, L.M. Cha, J. Mazumder, L.J. Song, Effects of laser modes on Nb segregation and Laves phase formation during laser additive manufacturing of nickel-based superalloy, Mater. Lett. 188 (2017) 260–262.
[11] P. Kontis, E. Chauvet, Z. Peng, J. He, A.K. da Silva, D. Raabe, C. Tassin, J.-J. Blandin, S. Abed, R. Dendievel, B. Gault, G. Martin, Atomic-scale grain boundary engineering to overcome hot-cracking in additively-manufactured superalloys, Acta Mater. 177 (2019) 209–221.
[12] J.H. Boswell, D. Clark, W. Li, M.M. Attallah, Cracking during thermal post-processing of laser powder bed fabricated CM247LC Ni-superalloy, Mater. Des. 174 (2019) 107793, https://doi.org/10.1016/j.matdes.2019.107793.
[13] W. Zhou et al., Inhibition of cracking by grain boundary modification in a non-weldable nickel-based superalloy processed by laser powder bed fusion, Mater. Sci. Eng., A 791 (2020) 139745.
[14] M.J. Donachie, S.J. Donachie, Superalloys A Technical Guide, ASM International, 2002.
[15] J.N. DuPont, J.C. Lippold, S.D. Kiser, Welding Metallurgy and Weldability of Nickel-Base Alloys, John Wiley & Sons, Inc., Hoboken, NJ, USA, 2009.
[16] S. Kou, Solidification and liquation cracking issues in welding, J. Miner. Met. Mater. Soc. (2003) 37–42.
[17] D. Dye, O. Hunziker, R.C. Reed, Numerical analysis of the weldability of superalloys, Acta Mater. 49 (4) (2001) 683–697.
[18] R.K. Sidhu, O.A. Ojo, M.C. Chaturvedi, Microstructural response of directionally solidified Rene 80 superalloy to gas-tungsten arc welding, Metall. Mater. Trans. A 40A (2009).
[19] M. Zhong, H. Sun, W. Liu, X. Zhu, J. He, Wenjin Liu, Xiaofeng Zhu, Jinjiang He, Boundary liquation and interface cracking characterizationin laser deposition of Inconel 738 on directionally solidifiedNi-based superalloy, Scr. Mater. 53 (2) (2005) 159–164.
[20] A.T. Egbewande, R.A. Buckson, O.A. Ojo, Analysis of laser beam weldability of Inconel 738 superalloy, Mater. Charact. 61 (5) (2010) 569–574.
[21] M.B. Henderson, D. Arrell, R. Larsson, M. Heobel, G. Marchant, Nickel based superalloy welding practices for industrial gas turbine applications, Sci. Technol. Weld. Join. 9 (1) (2004) 13–21, https://doi.org/10.1179/136217104225017099.
[22] D. Qian, J. Xue, A. Zhang, Y. Li, N. Tamura, Z. Song, K. Chen, Statistical study of ductility dip cracking induced plastic deformation in polycrystalline laser 3D printed Ni-based superalloy, Sci. Rep. 7 (1) (2017), https://doi.org/10.1038/s41598-017-03051-x.
[23] Y.M. Arata, Fukuhisa, Seiji Katayama, Solidification Crack Susceptibility in Weld Metals of Fully Austenitic Stainless Steels (Report II): Effect of Ferrite, P, S, C, Si and Mn on Ductility Properties of Solidification Brittleness, Osaka University, 1977.
[24] N.E.N.J.C. Lippold, Further investigations of ductility-dip cracking in high chromium, ni-base filler metals, Weld. World 51 (2007).
[25] F. Liu, X. Lin, G. Yang, M. Song, J. Chen, W. Huang, Fencheng Liu, Gaolin Yang, Menghua Song, Jing Chen, Weidong Huang, Microstructure and residual stress of laser rapid formedInconel 718 nickel-base superalloy, Opt. Laser Technol. 43 (1) (2011) 208–213.
[26] X. L. Fencheng Liu, Chunping Huang, Menghua Song, Gaolin Yang, Jing Chen, Weidong Huang, The effect of laser scanning path on microstructures and mechanical properties of laser solid formed nickel-base superalloy Inconel 718, 509 (2011) 4505–4509.
[27] L.X. Jianyin Chen, Sheng-Hui Wang, Experimental studies on process-induced morphological characteristics of macro- and microstructures in laser consolidated alloys, 46 (2011) 5859–5875, 2011, doi: 10.1007/s10853-011-5543-3.
[28] S. Imbrogno, A. Alhuzaim, M.M. Attallah, Influence of the laser source pulsing frequency on the direct laser deposited Inconel 718 thin walls, J. Alloys Compd. 856 (2021) 158095, https://doi.org/10.1016/j.jallcom.2020.158095.
[29] D. Gibson, R. Plume, E. Bergin, S. Ragan, N. Evans, Molecular Line Observations Of Infrared Dark Clouds. II. Physical Conditions, The Astrophysical 705 (1) (2009) 123–134.
[30] J.E. MacDonald, Hot Isostatic Pressing of A High Temperature Ni-Superalloy CM247LC: Processing-Microstructure-Properties Doctor of Philosophy, School Of Metallurgy and Materials, University of Birmingham, 2016.
[31] S. Raghavan, S.S. Sahay, Modeling the grain growth kinetics by cellular automaton, Mater. Sci. Eng., A 445-446 (2007) 203–209.
[32] Q. Zhang, The microstructure and properties of powder hipped nickel-based superalloy CM247LC, Metallurgy and Materials, University of Birmingham, 2011.
[33] J.M. Kikel, D.M. Parker, Ductility dip cracking susceptibility of filler metal 52 and alloy 690, Trends Weld. Res. (1998) 757–762.

[34] A.J. Haslam, S.R. Phillpot, D. Wolf, D. Moldovan, H. Gleiter, Mechanisms of grain growth in nanocrystalline fcc metals by molecular-dynamics simulation, Mater. Sci. Eng., A 318 (1-2) (2001) 293–312.
[35] R. Muñoz-Moreno, V.D. Divya, S.L. Driver, O.M.D.M. Messé, T. Illston, S. Baker, M.A. Carpenter, H.J. Stone, Effect of heat treatment on the microstructure, texture and elastic anisotropy of the nickel-based superalloy CM247LC processed by selective laser melting, Mater. Sci. Eng., A 674 (2016) 529–539.
[36] P.A. McNutt, An investigation of cracking in laser metal deposited nickel superalloy CM247LC, Department of Metallurgy and Materials, University of Birmingham, 2015.
[37] Y.T. Tang, C. Panwisawas, J.N. Ghoussoub, Y. Gong, J.W.G. Clark, A.A.N. Németh, D.G. McCartney, R.C. Reed, Alloys-by-design: Application to new superalloys for additive manufacturing, Acta Mater. 202 (2021) 417–436.
[38] X. Wang, L.N. Carter, N.J.E. Adkins, K. Essa, M.M. Attallah, Novel Hybrid Manufacturing Process of CM247LC and Multi-Material Blisks, Micromachines 11 (5) (2020) 492, https://doi.org/10.3390/mi11050492.
[39] J.E. MacDonald, R.H.U. Khan, M. Aristizabal, K.E.A. Essa, M.J. Lunt, M.M. Attallah, Influence of powder characteristics on the microstructure andmechanical properties of HIPped CM247LC Ni superalloy, Mater. Des. 174 (2019) 107796, https://doi.org/10.1016/j.matdes.2019.107796.
[40] ASM Handbook Fractography (2004).